Circular hole ENZ photonic crystal fibers exhibit high birefringence

TIANYU YANG,[1] CAN DING,[1*] RICHARD W. ZIOLKOWSKI,[1,2] AND Y. JAY GUO[1]

[1]*Global Big Data Technologies Centre, University of Technology Sydney, Sydney 2007, AU*
[2]*College of Optical Sciences, The University of Arizona, Tucson, AZ 85721-0104, USA*
**Corresponding author (Can.ding@uts.edu.au)*

Abstract—A novel photonic crystal fiber (PCF) design that yields very high birefringence is proposed and analyzed. Its significantly enhanced birefringence is achieved by filling selected air holes in the cladding with an epsilon-near-zero (ENZ) material. Extensive simulation results of this asymmetric material distribution in the lower THz range demonstrate that the reported PCF has a birefringence above 0.1 and a loss below 0.01 cm^{-1} over a wide band of frequencies. Moreover, it exhibits near zero dispersion at 0.75 THz for both the X- and Y-polarization modes and a birefringence equal to 0.28. This THz PCF is then scaled successfully to optical frequencies. While the high birefringence is maintained, this optical PCF has a very high loss in its Y-polarization mode and, consequently, yields single-polarization single-mode (SPSM) propagation, exhibiting near zero dispersion at the optical telecom wavelength of 1.55 μm. The ideal ENZ materials used for these conceptual models are replaced with realistic ones for both the THz and optical PCF designs. With the currently available ENZ materials, the realistic PCFs still have a high birefringence, but with higher losses compared to the idealized results. Future developments of ENZ materials that achieve lower loss properties will mitigate this issue in any frequency band of high interest.

OCIS codes: (260.1440) Birefringence; (060.2270) Fiber characterization; (060.2290) Fiber materials; (060.5295) Photonic crystal fibers.

References and links

1. A. Redo-Sanchez and X.-C. Zhang, "Terahertz science and technology trends," IEEE J. Sel. Topics Quantum Electron **14**(2), 260-269 (2008).
2. D. O. Otuya, K. Kasai, M. Yoshida, T. Hirooka, and M. Nakazawa, "A single-channel 1.92 Tbit/s, 64 QAM coherent optical pulse transmission over 150 km using frequency-domain equalization," Opt. Express **21**(19), 22808-28816 (2013).
3. K. Wang and D. M. Mittleman, "Metal wires for terahertz wave guiding," Nature **432**, 376-379 (2004).
4. J. A. Harrington, R. George, and P. Pedersen, "Hollow polycarbonate waveguides with inner Cu coatings for delivery of terahertz radiation," Opt. Express **12**(21), 5263-5268 (2004).
5. J. Li, K. Nallappan, H. Guerboukha, and M. Skorobogatiy, "3D printed hollow core terahertz Bragg waveguides with defect layers for surface sensing applications," Opt. Express **25**(4), 4126-4144 (2017).
6. P. St. J. Russell, "Photonic-Crystal Fibers," J. Lightw. Technol. **24**(12), 4729-4749 (2006).
7. G. K. M. Hasanuzzaman, M. S. Habib, S. M. A. Razzak, M. A. Hossain, and Y. Namihira, "Low loss single-mode porous-core Kagome photonic crystal fiber for THz wave guidance," J. Lightw. Technol. **33**(19), 4027-4031 (2015).
8. A. Aming, M. Uthman, R. Chitaree, W. Mohammed, and B. M. A. Rahman, "Design and characterization of porous core polarization maintaining photonic crystal fiber for THz guidance," J. Lightw. Technol. **34**(23), 5583-5590 (2016).
9. S. F. Kaijage, Z. B. Ouyang, and X. Jin, "Porous-core photonic crystal fiber for low loss terahertz wave guiding," IEEE Photon. Technol. Lett. **25**(15), 1454-1457 (2013).
10. J. Yang, B. Yang, Z. Wang, and W. W. Liu, "Design of the low-loss wide bandwidth hollow-core terahertz inhibited coupling fibers," Opt. Comm. **343**, 150-156 (2015).
11. M. Sharma, N. Borogohain, and S. Konar, "Index guiding photonic crystal fibers with large birefringence and walk-off," J. Lightw. Technol. **31**(21), 3339-3344 (2013).
12. A. Hassani, A. Dupuis, and M. Skorobogatiy, "Porous polymer fibers for low-loss terahertz guiding," Opt. Express **16**(9), 6340-6351 (2008).
13. K. Ahmed, S. Chowdhury, B. K. Paul, Md. S. Islam, S. Sen, Md. I. Islam, and S. Asaduzzaman, "Ultrahigh birefringence, ultralow material loss porous core single-mode fiber for terahertz wave guidance," Appl. Opt. **56**(12), 3477-3483 (2017).

14. S. Atakaramians, S. A. Vahid, H. Ebendorff-Heidepriem, M. Nagel, B. M. Fischer, D. Abbott, and T. M. Monro, "THz porous fibers: design, fabrication and experimental characterization," Opt. Express **17**(16), 14053-14062 (2009).
15. Islam, Md. S. Habib, G. K. M. Hasanuzzaman, R. Ahmad, S. Rana, andS. F. Kaijage, "Extremely high-birefringent asymmetric slotted-core photonic crystal fiber in THz regime," IEEE Photon. Technol. Lett. **27**(21), 2222-2225 (2015).
16. T.-Y. Yang, E. Wang, H. Jiang, Z. Hu, and K. Xie, "High birefringence photonic crystal fiber with high nonlinearity and low confinement loss," Opt. Express **23**(7), 8329-8337 (2015).
17. G. K. M. Hasanuzzaman, S. Rana, and M. S. Habib, "A novel low loss, highly birefringent photonic crystal fiber in THz regime," IEEE Photon. Technol. Lett. **28**(8), 899-902 (2016).
18. R. Islam, M. S. Habib, G. K. M. Hasanuzzaman, S. Rana, and M. A. Sadath, "Novel porous fiber based on dual-asymmetry for low-loss polarization maintaining THz wave guidance," Opt. Lett. **41**(3), 440-445(2016).
19. H. Chen, H. Wang, H. Hou, and D. Chen, "A terahertz single-polarization single-mode photonic crystal fiber with a rectangular array of micro-holes in the core region," Opt. Comm. **285**(18), 3726-3729 (2012).
20. J. Ju, W. Jin, and M. S. Demokan, "Design of single-polarization single-mode photonic crystal fiber at 1.30 and 1.55 μm," J. Lightw. Technol. **24**(2), 825-830 (2006).
21. X. Lin, H.-J. Zheng, C.-Q. Wu, and S.-L. Liu, "A novel single-polarization single-mode photonic crystal fiber with circular and elliptical air-holes arrays," Opt. Lett. **9**(2), 0120-0123 (2013).
22. J. Dai, J. Q. Zhang, W. L. Zhang, and D. Grischkowsky, "Terahertz time-domain spectroscopy characterization of the far-infrared absorption and index of refraction of high-resistivity, float-zone silicon," Opt. Soc. Am. B **21**(7), 1379-1386 (2004).
23. COMSOL Multiphysics®, COMSOL, Stockholm, Sweden. http://cn.comsol.com/rf-module.
24. R. W. Ziolkowski, "Propagation in and scattering from a matched metamaterial having a zero index of refraction," Phys. Rev. E Stat. Nonlin. Soft Matter Phys. **70**(4), 046608 (2004).
25. N. Engheta and R. W. Ziolkowski, *Metamaterials: Physics and Engineering Explorations* (Wiley, 2006).
26. A. Reyes-Coronado et al., "Self-organization approach for THz polaritonic metamaterials," Opti. Express **20**(13), 14663-14682 (2012).
27. G. V. Naik, V. M. Shalaev, and A. Boltasseva, "Alternative plasmonic materials: beyond gold and silver," Adv. Mater. **25**(24), 3264-3294 (2013).
28. A. Boltasseva, School of Electrical and Computer Engineering and Birck Nanotechnology Center, Purdue University, 1205 West State Street, West Lafayette, IN 47907-2057, USA (most recently obtained AZO values, private communication, 2018).
29. T.-Y. Yang, C. Ding, R. W. Ziolkowski, and Y. J. Guo, "A scalable THz ultra-high birefringence and ultra-low loss partially-slotted photonic crystal fiber," IEEE J. Lightw. Technol., early access, DOI: 10.1109/JLT.2018.2842825, (2018).
30. I. H. Malitson, "Interspecimen comparison of the refractive index of fused silica," J. Opt. Soc. Am. **55**(10), 1205-1209 (1965).
31. J. Ballato and P. Dragic, "Rethinking optical fiber: New demands, old glasses," J. Am. Ceram. Soc. **96**(9), 2675-2692, (2013).
32. J. Ballato and P. Dragic, "Materials development for next generation optical fiber," Materials **7**(6), 4411-4430 (2014).
33. M. A. Schmidt, A. Argyros, and F. Sorin, "Hybrid optical fiber – an innovative platform for in-fiber photonic devices," Adv. Optical Mater. **4**(1), 13-36 (2016).
34. C. Markos, J. C. Travers, A. Abdolvand, B. J. Eggleton, O. Bang, "Hybrid photonic-crystal fiber," Rev. Mod. Phys. **89**(4), 045003 (2017).
35. J. Hou, D. Bird, A. George, S. Maier, B. T. Kuhlmey, and J. C. Knight, "Metallic mode confinement in mircrostructured fibres," Opt. Express **16**(9), 5983-5990 (2008).
36. H. W. Lee, M. A. Schmidt, R. F. Russell, n. Y. Joly, H. K. Tyagi, P. Uebel, and P. St. J. Russell, "Pressure-assisted melt-filling and optical characterization of Au nano-wires in microstructured fibers," Opt. Express **19**(13), 12180-12189 (2011).
37. A. Amezcua-Correa, J. Yang, C. E. Finlayson, A. C. Peacock, J. R. Hayes, P. J. A. Sazio, J. J. Baumberg, and S. M.Howdle, "Surface-enhanced Raman scattering using microstructured optical fiber substrates," Adv. Funct. Mater. **17**(13), 2024-2030 (2007).
38. N. F. Baril, R. He, T. D. Day, J. R. Sparks, B. Keshavarzi, M. Krishnamurthi, A. Borhan, V. Gopalan, A. C. Peacock, N. Healy, P. J. A. Szio, and J. V. Badding, "Confined high-pressure chemical deposition of hydrogenated amorphous silicon," J. Am. Chem. Soc. **134**(1), 19-22 (2012).
39. R. He, P. J. A. Sazio, A. C. Peacock, N. Healy, J. R. Sparks, M. Krishnamurthi, V. Gopalan, and J. V. Badding, "Integration of gigahertz-bandwidth semiconductor devices inside microstructured optical fibres," Nat. Photonics **6**, 174-179 (2012).
40. G. V. Naik and A. Boltasseva, "A comparative study of semiconductor-based plasmonic metamaterials" Metamaterials **5**(1), 1-7 (2011).
41. P. R. West, S. Ishii, G. V. Naik, N. K. Emani, V.M. Shalaev, A. Boltasseva, "Searching for better plasmonic materials," Laser. Photon. Rev., **4**(6), 795-808 (2011).

42. V. Pacheco-Pena, N. Engheta, S. Kuznetsov, A. Gentselev, and M. Beruete, "Experimental realization of an epsilon-near-zero graded-index metalens at terahertz frequencies," Phys. Rev. Appl. **8**(3), 034036 (2017).
43. I. Liberal and N. Engheta, "Zero-index platforms: Where light defies geometry," Opt. Photonics News **27**(7), 26-33 (2016).
44. I. Liberal and N. Engheta, "Near-zero refractive index photonics," Nat. Photonics **11**, 149-158 (2017).

1. Introduction

Terahertz (THz) frequencies (wavelengths) are generally defined in the range from 0.1-10 THz (30-3000 μm). This segment of the electromagnetic spectrum has attracted substantial worldwide research attention in the last decade due to its impactful applications in sensing, imaging, communications, and security [1]. Advanced THz wave generation and detection technologies have been reported. However, most of the recently reported commercial THz systems are still based on free space propagation [2], mainly due to the lack of attractive THz waveguides. These free-space propagation-based systems usually suffer from unwanted absorption losses, difficulties in integration with other devices, and high sensitivity to the surrounding environment. Consequently, several types of THz waveguides have been proposed to replace free space propagation, including solid stainless wires [3], dielectric metal-coated tubes [4], and Bragg fibers [5]. However, they are all based on metallic wires and subwavelength dielectric fibers. As a result, most of the propagating fields reside outside of the waveguide core, which leads to a high propagation loss and undesired interactions with the exterior environment.

Photonic crystal fibers (PCFs) have been successfully deployed in the optical regime due to their performance advantages, including good confinement ability, low loss, tunable dispersion, and structural flexibility [6]. Recently, PCFs have also been advocated for THz applications [7-9]. There are three kinds of PCFs recently employed in the THz regime. One is a hollow core PCF whose wave guiding principles are based on photonic band gap properties [10]. While a substantial portion of the THz fields propagate in air with low losses in these PCFs, their bandwidths are narrow. A second kind is the solid core PCF whose wave guiding properties are based on total internal reflection (TIR) principles [11]. While the majority of the wave energy is transmitted within their solid cores, these PCFs usually have high losses because the materials used to construct them have high material absorption losses in the THz regime. The third kind of THz PCF is called a porous fiber; its operation is also based on TIR principles. Extra subwavelength air hole arrays are introduced into the core area of these porous fibers to concentrate the field energy in them, thereby minimizing the propagation losses [12].

Several key PCF characteristics must be considered for practical THz applications with loss as one of the most important factors. The loss in THz PCFs is mainly attributed to the effective material loss (EML) and the confinement loss (CL). Birefringence is another important factor for THz waveguides. High birefringence is desired for polarization-based THz guiding, sensing, filtering, and splitting applications. In particular, highly birefringent PCFs maintain the polarization state of the fields propagating in them. Two other crucial PCF factors for communication applications are the bandwidth and dispersion. A wide operational bandwidth and, hence, an enhanced information capacity is preferred. Additionally, flat dispersion over a wide bandwidth mitigates high bit error rates.

The most widely used approach to introduce birefringence into THz PCF designs is to geometrically break the symmetry within their holey claddings and/or core areas. One direct way to realize a high birefringence PCF is to introduce shaped air holes that have different effects on the X- and Y-polarized fields propagating in it. Examples include elliptical and rectangular air holes. Squeezed elliptical holes were etched in the core area of the PCF introduced in [13]. A birefringence on the order of 10^{-2} was achieved with a low EML = 0.069 cm^{-1}. A highly birefringent PCF employing rectangular air holes was considered in [14]. A fabricated and tested prototype attained a birefringence of 0.012 at 0.65 THz and a reasonable EML below 0.25 cm^{-1} for frequencies below 0.8 THz. A higher birefringence, 0.075, with a low EML of 0.07 cm^{-1} was realized at 1.0 THz in [15] with a PCF that employed rectangular

air slots in its core. However, the intrinsically asymmetric elliptical and rectangular holes in these designs are difficult to implement practically due to their more complex geometrical structure.

Compared to elliptical and rectangular holes, circular holes are much easier to fabricate. Asymmetric sets of circular air-holes in the cladding and core regions of the PCFs developed in [16-18] achieved high birefringence values. [16] utilized asymmetrical circular air-holes in both the cladding and the core region of the reported PCF, resulting in a birefringence of 0.026, and a low CL of 10^{-5} dB/m. The dual-hole unit-based porous-core hexagonal PCF in [17] attained a birefringence of 0.033, an EML of 0.43 dB/cm, and a CL of 10^{-3} dB/m at an operating frequency of 0.85 THz. The multi-hole core PCF in [18] achieved a higher birefringence = 0.045, a low EML = 0.08 cm^{-1}. Nevertheless, although PCFs based on circular holes are easier to fabricate, they have not been able to achieve a birefringence as high as those based on asymmetric rectangular holes or elliptical holes. This drawback is due primarily to the way that birefringence was introduced into them. The state-of-the-art birefringence of these asymmetric core-cladding circular hole-based PCFs is limited to be barely above 0.1.

Because their birefringence values are not as high as desired, the polarization maintaining ability of these birefringent PCFs remains affected by polarization cross talk and polarization mode dispersion. One immediate way to overcome this problem is to further enhance the birefringence. Another is to eliminate one transmission mode and attain a single-polarization single-mode (SPSM) PCF by introducing noticeable loss differences between the X- and Y-polarized propagating modes [19-21]. SPSM PCFs are desirable; they mitigate polarization cross talk and mode dispersion issues.

In this paper, a THz PCF with circular elements is developed to attain very high birefringence values. The high index contrast between the propagating X- and Y-polarized modes is realized by not only breaking the symmetry of the overall geometrical structure, but also loading certain of its circular air holes with materials having different refractive indexes (n). In particular, specific holes in the first ring of the cladding are filled with an epsilon-near-zero (ENZ) material ($n=0.1$) and with air ($n=1.0$). The background and, hence, core material is high resistivity silicon (HRS) with a high refractive index ($n=3.417$) [22]. Parameter sweeps of the key dimensions are presented to illustrate how the design can be optimized to have the best birefringence and loss characteristics. The simulation results demonstrate that with ideal ENZ materials the proposed PCF achieves a very high birefringence near 0.3, an ultra-low loss below 10^{-2} cm^{-1}, and zero dispersion for frequencies around 0.75 THz for both the propagating X- and Y-polarized fields. Moreover, this model PCF also exhibits excellent performance when it is scaled to the optical regime. The corresponding optical PCF model not only has excellent birefringence, loss, and dispersion properties, but it also enables SPSM propagation across a wide band. Finally, realistic ENZ materials are introduced into the THz and optical PCF models. The performance characteristics of these realistic PCFs are re-assessed. The simulation results demonstrate that good birefringence values are maintained but with increased losses. While this first step demonstrates that the introduction of ENZ materials into PCF designs facilitates very interesting performance characteristics, the next step will be the realization of ENZ-based PCFs when appropriately lower loss ENZ materials become available.

The reminder of this paper is organized as follows. Section 2 introduces two complementary PCF configurations and their design parameters. These two complementary configurations are then studied and compared in Section 3. One model is selected based on its performance characteristics and is then optimized for the THz regime in Section 4. Next, this optimized THz PCF model is scaled in Section 5 to the optical regime. In Section 6, the performance characteristics of both the THz and optical PCFs with realistic ENZ materials are recalculated and discussed. Potential methods to realize the reported ENZ-based THz and optical PCF designs will be discussed. Finally, the paper is concluded in Section 7.

All of the simulations in this work were conducted with the COMSOL Multiphysics commercial software package [23]. The fields associated with each numerical model were obtained with its full-wave, vector finite element method (FEM). Furthermore, each simulation region was truncated with its perfectly matched layer (PML) absorbing boundary condition to strongly attenuate any numerical reflections arising from its outer boundaries. Note that only the fundamental propagation modes were considered to obtain the simulation results reported here. It was found in the initial studies of each configuration that most of the higher order modes suffer from very high propagation losses and dissipate rapidly. Consequently, they have no impact on the reported results.

2. THz PCF configurations

Figures 1(a) and 1(b) show the cross sectional views of two complementary PCF configurations, here denoted as Type 1 and Type 2, respectively. While they have identical physical arrangements, they have different asymmetric material distributions. Unlike the previously advocated porous-core PCFs [13-15, 17, 18], these PCFs have solid cores and, hence, would be easier to fabricate. A triangular lattice distribution of five air-hole rings defines their claddings. The core circle and only the two adjacent circular holes (shadow highlighted) have the diameter d_2. All of the other circular holes have the diameter d_1. The distance between any two adjacent holes in the cladding is the lattice constant Λ. A perfect matching layer with a thickness that is 10% of the whole diameter of the PCF is placed concentrically on the outside of the hole-based cladding region. The Type 1 and Type 2 PCFs shown in Figs. 1(a) and 1(b) have, respectively, four holes and two holes filled with ENZ material. The background material and, hence, the core is HRS. The HRS was selected because of its outstanding properties including its low bulk material absorption loss < 0.01 cm^{-1} from 0.1-1 THz and its stable refractive index $n = 3.417$ in the frequency range from 0.5-4.0 THz [22]. Materials with ENZ properties can be attained with metamaterials [24, 25] or with naturally occurring materials [26-28]. In this work, ideal ENZ material is used first. Its real part of refractive index is set to 0.1 and the imaginary part (material loss) is set to zero in the frequency range of interest. Later, in section 6, realistic ENZ materials will be introduced to replace the ideal ones. These THz and optical PCFs are then re-simulated to provide more appropriate representations of the performance characteristics of a potentially fabricated prototype.

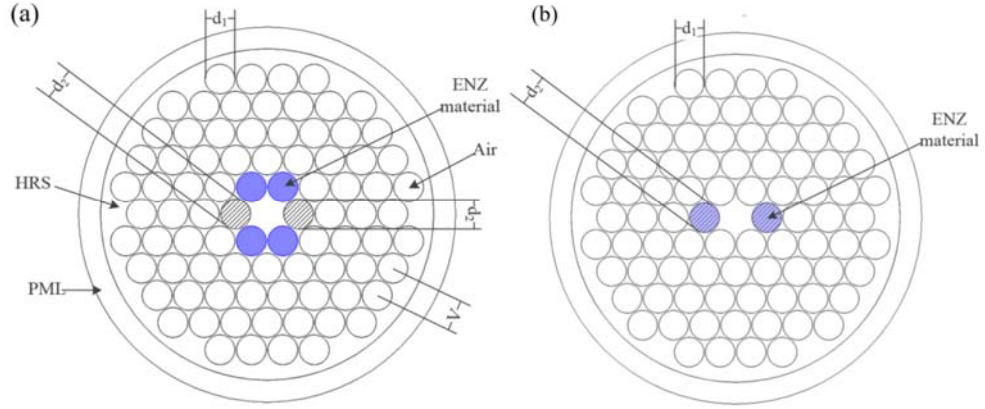

Fig. 1. Cross sectional view of the complementary PCFs. (a) Type 1. (b) Type 2.

3. Comparison of the type 1 and type 2 PCFs

A high birefringence is attained with the Type 1 and Type 2 PCFs because they not only break their geometric symmetry, but also have an asymmetric refractive index distribution. The geometrical asymmetry has been introduced simply with the change in the diameter (d_2) of the

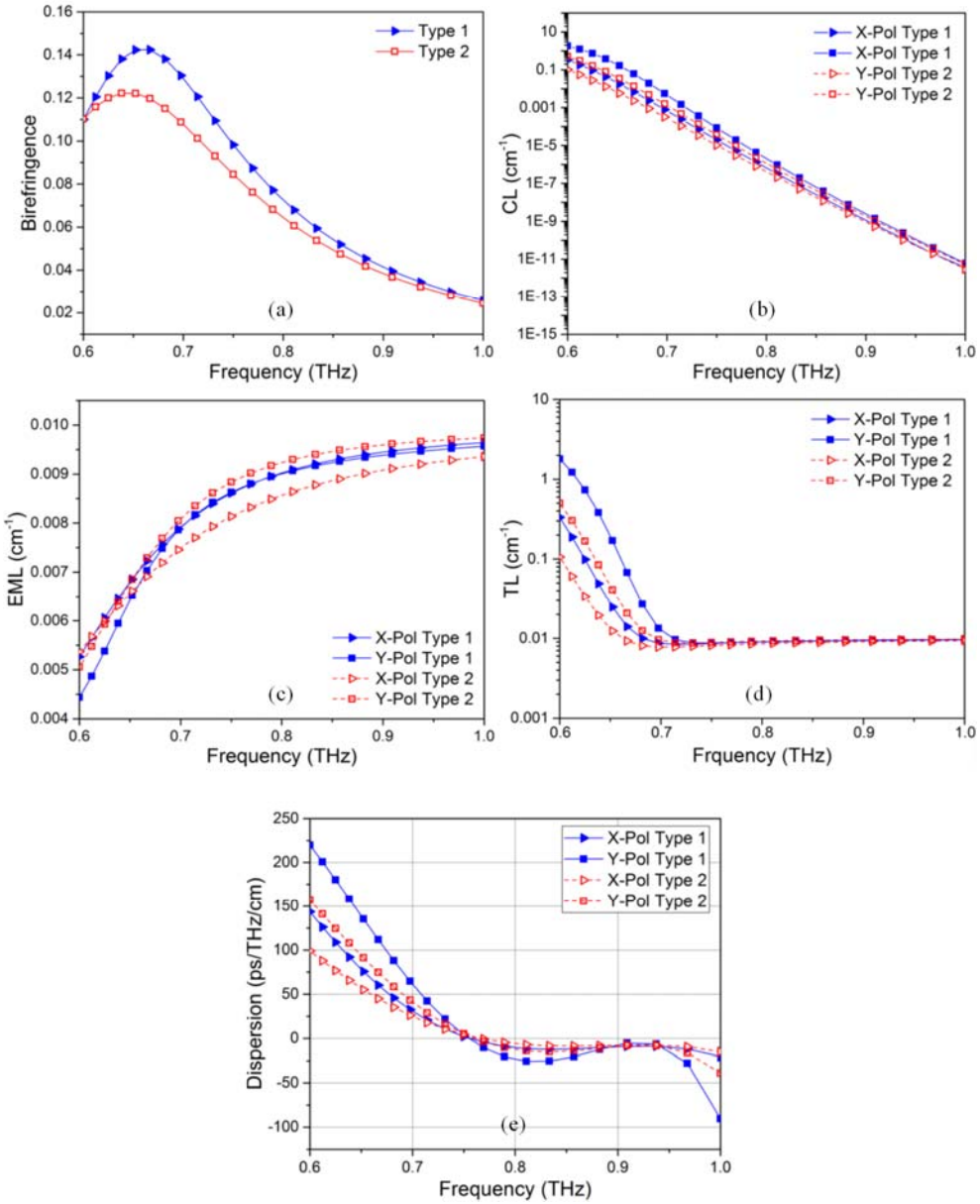

Fig. 2. Comparisons of the performance characteristics of the Type 1 and Type 2 PCFs. (a) Birefringence. (b) CL. (c) EML. (d) TL. (e) Dispersion.

selected two air holes. Moreover, they both have an asymmetric refractive index distribution since the ENZ material is introduced only into select air holes.

To determine which of the two PCFs designs is a better candidate, we first considered both of them with all of their hole diameters set to be the same, i.e., we set $d_1 = d_2 = 0.95\Lambda$, where

the distance between their centers was taken to be $\Lambda = 80$ μm. The ENZ filled holes shown in Fig. 1 were maintained. A variety of simulated performance characteristics of these geometrically symmetric but refractive index asymmetric structures were obtained. The key performance characteristics of interest here include the birefringence, CL, EML, total loss (TL), and dispersion. Their values for both types of PCFs are compared, respectively, in Figs. 2(a) to 2(e).

The birefringence shown in Fig. 2(a) was calculated as

$$B = \left|n_x - n_y\right|, \tag{1}$$

where B denotes the birefringence, and n_x and n_y represent the modal effective indices for the X- and Y-polarizations, respectively. The CLs shown in Fig. 2(b) were calculated as [7]

$$L_c(cm^{-1}) = \frac{4\pi f}{c} \times Im\left[n_{eff}\right], \tag{2}$$

where c is the speed of light in vacuum and $Im[n_{eff}]$ is the imaginary part of the effective refractive index. The EML values plotted in Fig. 2(c) were obtained with the expression:

$$\alpha_{eff}(cm^{-1}) = \frac{\left(\frac{\varepsilon_0}{\mu_0}\right)^{\frac{1}{2}} \int_{mat} n_{mat}\alpha_{mat}|E|^2 dA}{2\int_{All} S_z dA}, \tag{3}$$

where ε_0 and μ_0 are the vacuum permittivity and permeability, α_{mat} is the bulk material absorption loss, n_{mat} is the refractive index of the background material, E is the modal electric field, and S_z is the Poynting vector projected along the Z (propagation) direction. The total loss (TL) values given in Fig. 2(d) represent the sums of the CL and EML. The dispersion

results shown in Fig. 2(e) were attained only considering the waveguide dispersion since the material dispersion of the HRS is negligible within the desired frequency range, 0.5 to 4.0 THz. They were calculated as [7]

$$\beta_2 = \frac{2}{c}\frac{dn_{eff}}{d\omega} + \frac{\omega}{c}\frac{d^2 n_{eff}}{d\omega} \tag{4}$$

where n_{eff} is the effective refractive index of the fundamental mode and $\omega = 2\pi f$ is the angular frequency of the source.

As shown in Fig. 2(a), both types of PCFs exhibit a very high birefringence. This feature is attributed to the noticeable difference between the refractive index of air ($n_{air} = 1.0$) and the ENZ material ($n_{ENZ} = 0.1$). In fact, the high birefringence values are realized even without breaking the geometric symmetry. Even higher birefringence is attained if it is broken by setting $d_2 \neq d_1$. Figure 2(b) illustrates that the two types of PCFs have similar ultra-low CL values for both the X- and Y-polarized fields. Furthermore, since the refractive index contrast between the cladding and core is significant, the field energy is well confined to the very low loss HRS core region. Figure 2(c) indicates that the EML values of both PCF types are very low and close to the material absorption loss values. This behavior further proves that most of the power is propagating in the solid core. It is also noted that the Type 1 PCF has its EML values larger and smaller, respectively, than those of the Type 2 PCF for the X- and Y-polarized modes. This behavior is associated with the different refractive index contrasts between the cladding and the core in those directions. For example, the Type 1 PCF has a more significant index contrast between the cladding and the core ($n_{ENZ} = 0.1 / n_{HRS} = 3.417$) for X-polarized modes than does the Type 2 PCF ($n_{air} = 1.0 / n_{HRS} = 3.417$). This aspect causes more energy to be confined in the core of the Type 1 PCF and, hence, results in a higher EML value. Nevertheless, its EML

values remain very low in the frequency range of interest because of the very low material loss property of the HRS. Figure 2(d) plots the TL values, i.e., the sum of the CL and EML values. Since the TL is a more comprehensive factor to assess the overall loss property of a PCF design, only the TL results will be given in following sections. Figure 2(e) shows the dispersion values versus frequency for the X- and Y-polarized modes of the two PCF types. It is observed that all of the dispersion curves are quite flat from 0.71 to 1.0 THz. More importantly, the cross-over points of the two polarization modes are near zero dispersion (around 0.75 THz) for both PCF types. To be specific, the values of the dispersion at the cross-over points are 0.7 and 3.5 ps/THz/cm for the Type 1 PCF and Type 2 PCF, respectively.

In summary, it was found that the overall performance characteristics of the two PCF types were quite similar, especially in the frequency range from 0.71 to 1.0 THz. Nonetheless, we selected the Type 1 PCF to conduct further studies for the following reasons. First, the Type 1 PCF exhibits a higher birefringence, which is the main concern of this work. Second, the dispersion cross-over point of the X- and Y-polarized modes is closer to zero for the Type 1 PCF. Finally, the TL values of the Type 1 PCF are no worse than those of the Type 2 PCF across the same frequency range, 0.71 to 1.0 THz.

4. Simulated performance of the THz PCF

Parameter sweeps were conducted to optimize the Type 1 PCF design in the frequency range, 0.71 to 1.0 THz, to achieve an ultra-high birefringence, low loss, and flat dispersion. A summary of the main design parameter results is given below. Guidelines for the future design efforts are also provided.

4.1 Effect of the lattice constant Λ

The most important design parameter is the lattice constant, Λ. All of the PCF dimensions are defined in proportion to it. A parameter sweep of Λ was conducted by changing its value from 70 to 90 μm with all of the other dimensions fixed relative to it, e.g., $d_1 = d_2 = 0.95\Lambda$. The computed birefringence, TL, and dispersion values for these different lattice constants are plotted in Figs. 3(a) and (b), respectively. As shown in Fig. 3(a), the birefringence of the proposed PCF for different Λ have similar tendencies, except when Λ = 70 μm. The birefringence is quite high in the lower portion of the frequency range before it starts to decrease as the frequency increases. Generally, it was found that the birefringence is larger when Λ is smaller. Additionally, because the HRS has a stable refractive index over these frequencies, the optimized PCF and its high birefringence values are "scalable" to other frequency regimes [29].

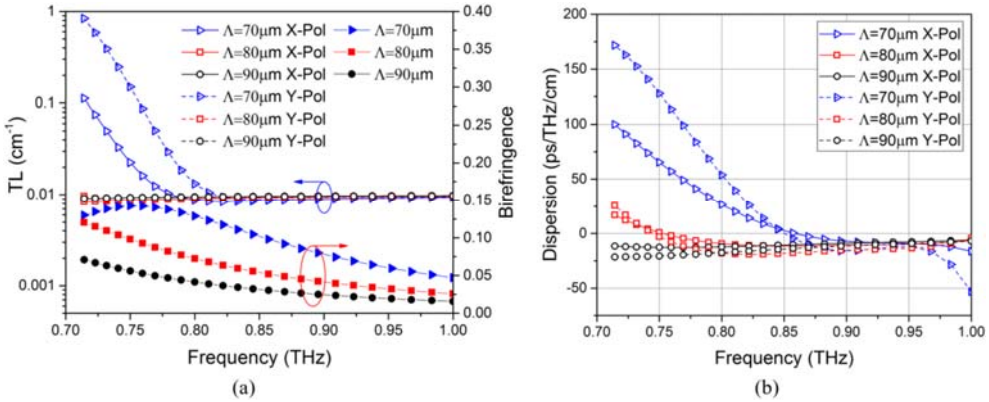

Fig. 3. Simulated PCF performance characteristics for different lattice constants and for both the X- and Y-polarized modes as functions of the source frequency. (a) Birefringence and TL values. (b) Dispersion values.

Figure 3(a) also shows the simulated TL values for different Λ. When Λ = 80 or 90 μm, the PCF has very low and stable TL values, i.e., near 0.01 cm^{-1}, across the frequency band of interest. For these cases, the loss is dominated by the EML since the power is well confined in the core. However, when Λ is reduced to 70 μm, a much higher loss is observed at the lower frequencies. This behavior is due to the dramatic increase of the CL, which in turn occurs because the PCF has a limited confinement ability when its Λ is smaller. Furthermore, as observed from Fig. 3(b), the PCF has a rather flat dispersion curve across the band of interest with larger Λ. Consequently, these parameter studies indicate that one must make some compromises when selecting the design parameters. Different choices lead to optimizing different combinations of the figures of merit, i.e., the values of the birefringence, TL, and dispersion. In this work, Λ was selected to be 80 μm. This choice provided a balanced performance. To be specific, the birefringence is > 0.026 from 0.71 to 1.0 THz and reaches its peak value, 0.12, at 0.71 THz. The losses are < 0.01 cm^{-1} across the entire frequency range. Moreover, the zero dispersion point occurs near 0.75 THz for both the X- and Y-polarized modes.

4.2 Effect of the diameter d_2

The birefringence can be further increased by introducing geometrical asymmetry. As shown in Fig. 2(a), if the diameter of the ENZ holes (d_1) is reduced, the effective refractive index of the Y-polarized mode will increase while that of the X-polarized mode will remain unchanged. This behavior leads to a reduction in the birefringence values. Therefore, it is found that reducing d_2 is the only approach to achieving higher birefringence values. Another simulation series was performed in which d_2 was swept from 0.7Λ to 0.9Λ with d_1 fixed at 0.95Λ and Λ = 80 μm. The calculated birefringence, TL, and dispersion values are presented in Fig. 4.

As shown in Fig. 4(a), a smaller d_2 results in a significant improvement in the birefringence values. The minimum and maximum birefringence across the band increase from 0.057 to 0.139 and from 0.205 to 0.395, respectively, when d_2 is reduced from 0.9Λ to 0.7Λ. On the other hand, while the losses are increased, the increment is minor and the TL remains below 0.01 cm^{-1} across the band. As shown in Fig. 4(b), a smaller value of d_2 also leads to a more flattened dispersion curve across the band for both polarizations. Moreover, the cross-over point of the X- and Y-polarized dispersion values is closer to the zero dispersion point. Note that although a smaller d_2 leads to the indicated enhanced performance, it was found that higher order mode propagation can no longer be neglected when considering short range propagation applications if d_2 becomes as small as 0.7Λ. Therefore, in this work, we chose d_2 = 0.8Λ. The resulting PCF has good performance characteristics while suppressing all higher order propagating modes. It is further noted that even higher birefringence could be obtained with the optimized PCF if higher order mode propagation is acceptable, as it can be in some specific applications.

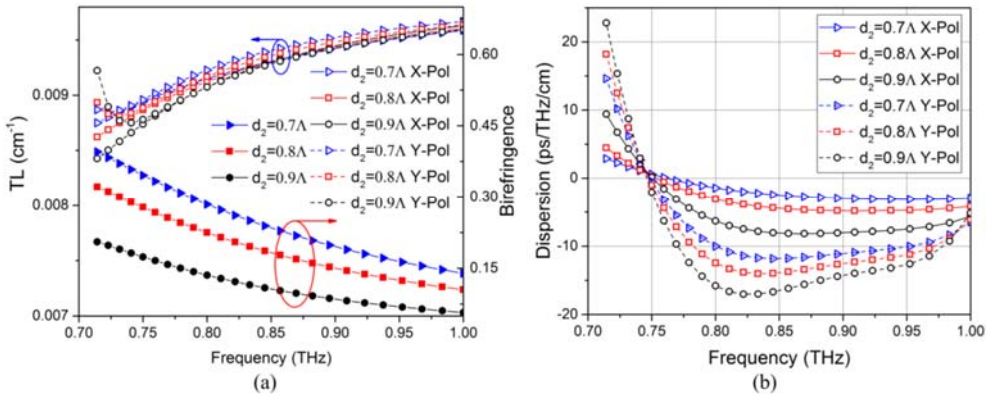

Fig. 4. Simulated performance characteristics of the geometrically and material asymmetric PCF as functions of the source frequency for different d_2 and for both the X- and Y-polarized modes. (a) Birefringence and TL values. (b) Dispersion values.

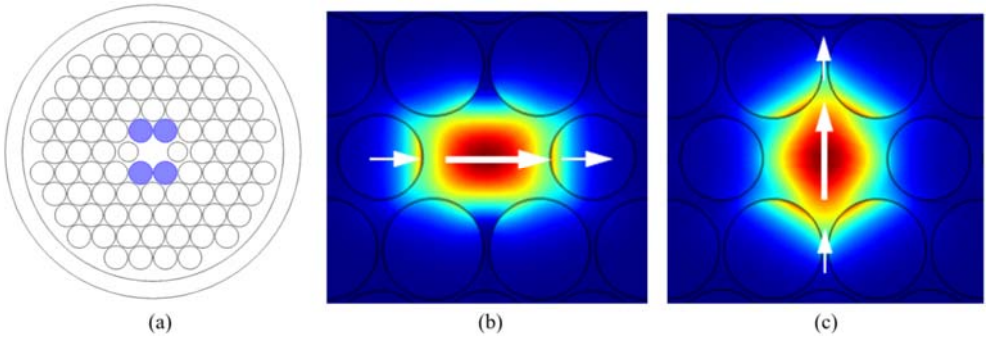

Fig. 5. Optimized PCF. (a) Optimal configuration. Distributions of the magnitude of the electric field intensity distribution for the (b) X- and (c) Y-polarized modes. The white arrows designate the polarization direction. Blue represents low values; red represents high values.

4.3 Optimized PCF

The optimized PCF has Λ = 80 μm, d_1 = 0.95Λ, and d_2 = 0.8Λ. Figure 5 shows the physical configuration and simulated distribution of the magnitude of the electric field intensity. As shown in Figs. 5(b) and 5(c), the field energy is well confined in the core region for both the X- and Y-polarized modes. The simulated TL, birefringence, and dispersion values for this optimized PCF across the 0.71 to 1.0 THz band are presented in Fig. 6. The birefringence values are high, above 0.1 across the band with a maximum value of 0.32 at 0.71 THz. The TL values are below 0.01 cm^{-1} across the band. Moreover, at 0.75 THz, both the X- and Y-polarized propagating modes experience near zero dispersion with a very high birefringence value of 0.28.

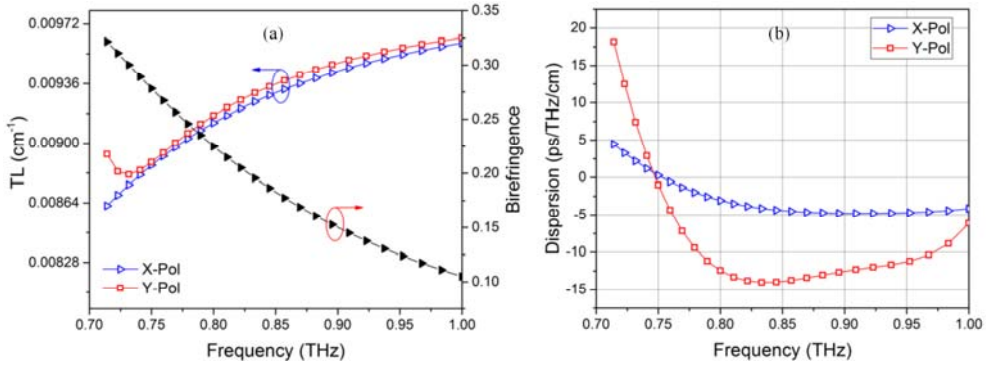

Fig. 6. Simulated performance characteristics of the optimized PCF as functions of the source frequency. (a) Birefringence and TL values. (b) Dispersion values.

5. Optical PCF

The optimized THz PCF shown in Fig. 5(a) was scaled to the optical regime [29]. Following the presented parameter optimization approach, an optical PCF was obtained with Λ = 0.95 μm, d_1 = 0.95 Λ, and d_2 = 0.8 Λ. While the optical PCF has the same configuration as the THz PCF, it has a different background material. The HRS does not have acceptable material properties in the optical regime. Silica was selected instead as the background material. It is essentially transparent in optical regime, thus allowing one to neglect the EML. The refractive index of silica was determined by the Sellmeier equation [30]. Substituting the result into Eqs. (1), (2), and (4), one can then calculate the birefringence, CL, and dispersion values of the optical PCF. Note that the group velocity dispersion coefficient, which nicely describes the chromatic dispersion in the optical regime, will be reported here since it is normally used to portray the dispersion properties of an optical PCF [6].

Figure 7 plots the simulated birefringence, TL, and dispersion values of the optimized optical PCF as functions of the source frequency. A high birefringence, 0.075, and a low TL value, 0.12 dB/m, were obtained for the X-polarized propagating modes at an operating wavelength of 1.55 μm. The TL value for the Y-polarized propagating modes was 47.3 dB/m. Consequently, since the Y-polarized modes exhibit a much higher loss than their X-polarized counterparts, the ratio of their TL values is greater than 143 from 1.50 μm to 1.74 μm. Consequently, this optical PCF acts a SPSM PCF. Furthermore, both the X- and Y-polarized modes experience near zero dispersion at 1.55 μm.

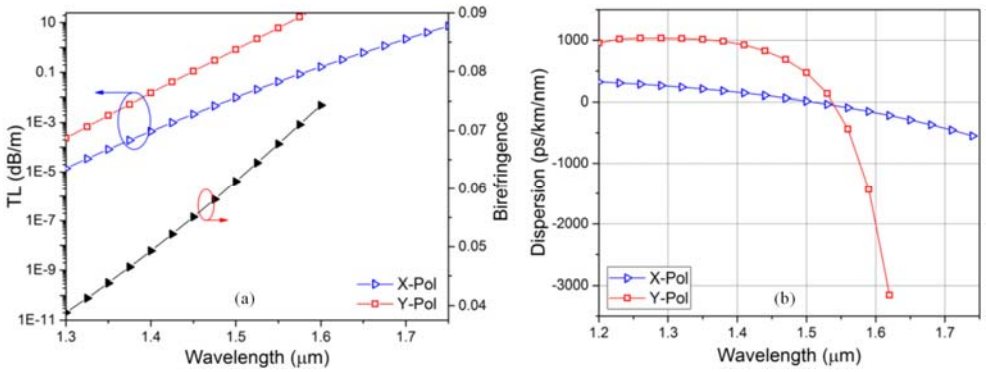

Fig. 7. Simulated optical PCF performance characteristics for both the X- and Y-polarized modes as functions of the source frequency. (a) Birefringence and TL values. (b) Dispersion values.

6. Realistic THz and optical PCFs

Having demonstrated that the idealized ENZ material properties lead to both THz and optical PCFs that exhibit high birefringence, low loss, and near zero dispersion properties, it was desired to investigate whether there are real or artificial materials that could provide those or nearly those ENZ properties. We have tried several known ENZ materials for our design. Unlike the idealized ENZ materials which have near-zero real ($\varepsilon_r \sim 0$) and zero imaginary permittivity value ($\varepsilon_i = 0$), these realistic ones have their ENZ crossover points at different frequencies and their losses (ε_i) are high. Consequently, some trade-offs had to be managed. It was found that high purity KCl [26] is a good candidate for the THz PCF with its ENZ crossover point near 6.3 THz. The investigated material for the optical PCF was AZO [27, 28]; it has its ENZ crossover point at optical frequencies near 1556 nm.

The key factor to attain the theoretically high birefringence is the presence of the ideal ENZ material in the optimized asymmetric configuration. These choices led to the very high index difference between the X and Y directions. The lower the ε_r value with no loss, the higher the impedance and index contrast becomes. Thus, essentially no electric field penetrates into those cylinders filled with the ideal ENZ medium. On the other hand, ε_i represents the loss property of the material. If it is high, the impedance and index contrasts decrease greatly, and the electric field penetrates into the cylinders. Thus, a higher ε_i value in the PCF structure produces worse loss properties over longer distances.

As illustrated in the Fig. 8, KCl attains its ENZ properties in the frequency range from 6.2 to 6.3 THz, where $\varepsilon_r \sim 0$ and ε_i is reasonably small. Replacing the background material with Topas, which has a refractive index of n=1.53 and an absorption loss of 2.0 cm^{-1} near 6.3 THz, the simulated birefringence, TL, and dispersion values of the resultant ENZ PCF are shown in the Fig. 9 for different lattice periods Λ. Specifically selecting Λ to be 25 μm optimizes the trade-offs between these performance characteristics. The TL and dispersion values are 12.7 cm^{-1} and -2.3 ps/THz/cm for the X-polarized mode, and 41.3 cm^{-1} and -10.1 ps/THz/cm for the Y-polarized mode, respectively. The birefringence value 0.105 at 6.2 THz is reasonable in comparison to the ideal value 0.28 and larger than most current PCFs. Since the confinement loss is negligible in comparison to the absorption loss, the relatively high TL value, 12.7 cm^{-1}, at 6.2 THz is due to the fact that the electric field now penetrates into the lossy ENZ holes, increasing the overall loss.

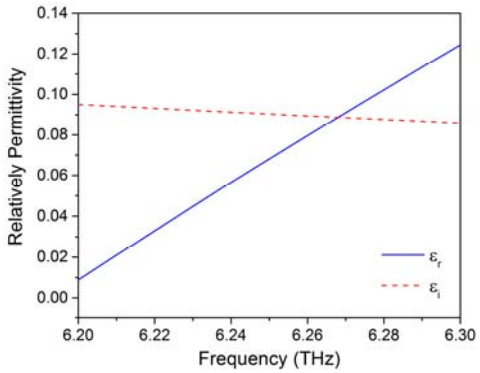

Fig. 8. The real and imaginary parts of the relative permittivity of 99.5 % pure KCl as functions of the source frequency.

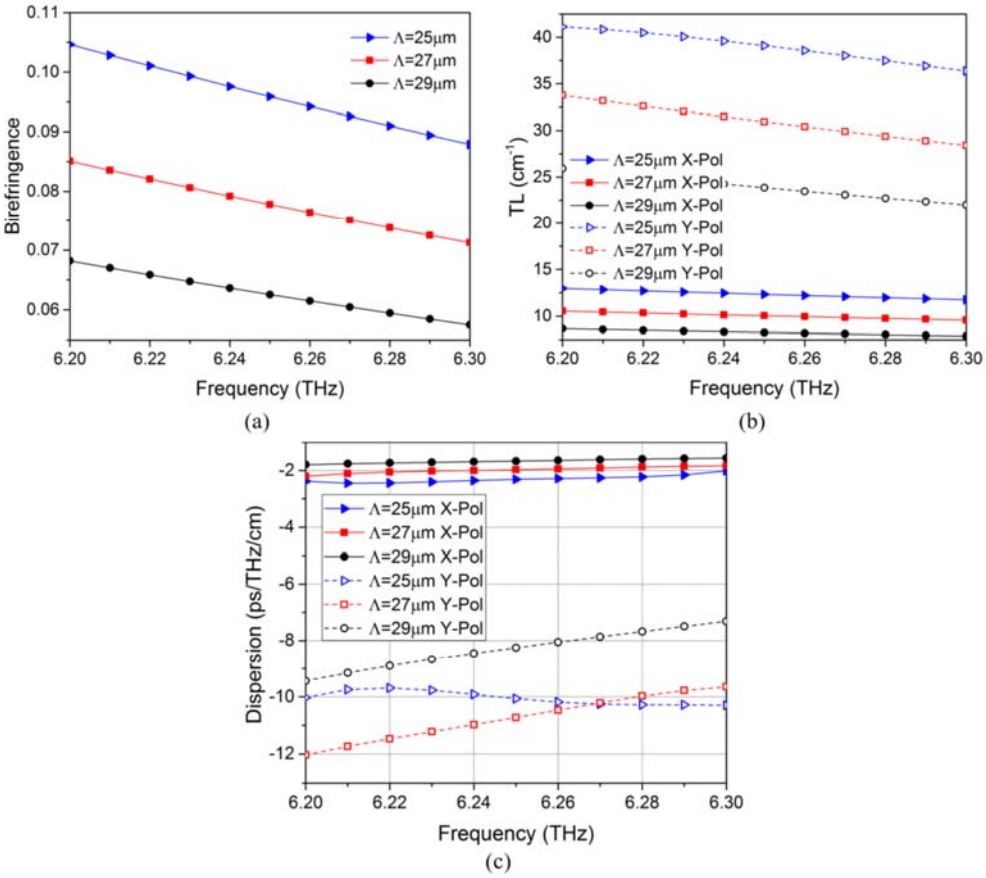

Fig. 9. Simulated properties of the THz PCF designed with KCl and Topas for different lattice periods Λ. (a) Birefringence. (b) TL. (c) Dispersion.

For the optical PCF, AZO was found to be suitable for C band (1530-1565 nm) operation. AZO has $\varepsilon_r \sim 0$ near 1550 nm, but $\varepsilon_i \sim 0.3$, which leads to a rather high absorption loss. Nevertheless, by choosing Λ as 0.95 μm, an AZO-based optical ENZ PCF still achieves a high birefringence, e.g., 0.0703 at 1550 nm, and flat dispersion across the band from 1545 to 1555 nm with TL ~ 0.5 dB/μm. The birefringence values of the optical PCF and the relative permittivity of a recently measured low loss AZO sample [28] used to calculate them are shown in Fig. 10.

Compared with the ideal cases, the obtained PCFs with realistic ENZ materials still achieve a relatively high birefringence. However, the losses are much higher due to the large ε_i values of the materials. At the current stage of material development, the proposed ENZ-based PCFs may find their immediate applications in the THz range and for short distance optical transmission applications. Clearly, the results shown in Figs. 9 and 10 are not near the idealized results. The limitations of the realistic ENZ-based PCFs are not due to the real part, but arise from the imaginary part of the ENZ permittivity. As long as $\varepsilon_r < 0.5$, a high birefringence can be obtained. Nonetheless, a much smaller ε_i is required to achieve low loss, especially in the optical bands. Luckily, the development of ENZ materials is of significant current interest and progress in improving their properties is occurring, e.g., [28]. This first step to combine ENZ materials into PCF designs has shown quite interesting and useful performance characteristics.

We await yet the realization of lower loss ENZ materials in the bands of high interest to attempt any realistic PFC fabrication and measurements based on our designs.

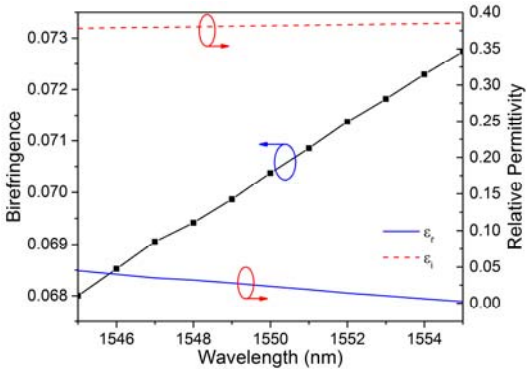

Fig. 10. The relative permittivity of AZO and the birefringence values of the optical PCF designed with AZO in the C band.

Practical implementations of ENZ materials into structured fibers can be accomplished with techniques introduced to realize optical fibers with more complex material compositions [31, 32] and hybrid optical fibers [33, 34]. One could simply insert naturally occurring bulk materials having ENZ properties directly into a structured fiber using direct thermal drawing [35], pressure-assisted melt filling techniques [36], or chemical depositions [37-39]. Our reported PCF designs could be achieved using the pressure-assisted melt filling technique to insert the bulk-form of KCl [26] or semi-conductor plasmonic materials [40] into the appropriate holes in the host silicon material for the THz PCF. Similarly, it could also be used to insert the bulk-form of Ag or K [41] into the appropriate holes in the host silica material for the optical version. An attractive alternative that could provide even more flexibility in the reported designs would be to replace the bulk ENZ materials with ENZ metamaterials, i.e., artificial materials engineered to attain the requisite ENZ properties at specified frequencies [42]. Methods for integrating metamaterials into structured fibers were reported in [33, 35]. Because of the strong recent interest in ENZ materials [43, 44] and their applications, it is anticipated that many more naturally occurring and artificially realized ENZ materials and even more advanced implementation techniques will be available in the near future, making the realization of the reported PCFs even more practical.

7. Conclusion

This paper demonstrated a PCF design that achieves very high birefringence, low loss, and near zero dispersion characteristics in both the THz and optical regimes. While its configuration is essentially a simple circular hole, triangular lattice, the enhanced performance characteristics were facilitated by introducing localized asymmetries in its geometry and material distribution. Most importantly, it takes significant advantage of loading several circular holes next to the core region with a material that exhibits ENZ properties in the operational band and changing the diameter of two holes in the overall structure. Two types of PCFs with complementary configurations were first investigated and compared. One design was selected to conduct further studies. Parameter sweeps of its key dimensions were conducted to obtain the optimized results and reported to provide design guidelines. From 0.71 to 1.0 THz, very high birefringence, i.e., greater than 0.1, was achieved with low loss, i.e., less than 0.01 cm^{-1} over this band. This THz PCF also exhibit near zero dispersion around 0.75 THz for both the X- and

Y-polarized propagating modes. This THz PCF was scaled to the optical regime. It was demonstrated that the resulting optical PCF has similar high birefringence and near zero dispersion values at the telecom wavelength, 1.55 μm, but with significantly different loss values for the X- and Y-polarized propagating modes. Hence, it realizes a very desirable SPSM property at optical frequencies.

The ideal ENZ material in the PCF design was replaced with realistic materials for both the THz and optical frequency regimes. Simulated performance characteristics of these realistic THz and optical PCF models were presented and discussed. The results show that, with currently available ENZ materials, high birefringence can still be obtained but the losses are much higher than those of the ideal cases. The high losses are attributed to the large imaginary part of the permittivity ε_i of the materials. We anticipate that future realizations of ENZ materials will become available with much lower losses in the frequency bands of high interest. Fabrication of the corresponding PCFs based on the designs reported here and the subsequent measurements to confirm their attractive performance characteristics await their eventual appearance.

Funding

Australian Research Council (ARC) (DP160102219).

Acknowledgments

The authors thank Prof. Alexandra Boltasseva and Mr. Clayton DeVault, Purdue University's Birck Nanotechnology Center, for sharing their very recently obtained AZO material parameters that were used in the realistic optical PCF calculations.